Research Square

Preprints are preliminary reports that have not undergone peer review.
They should not be considered conclusive, used to inform clinical practice,
or referenced by the media as validated information.

Development of a Multifunctional Fe_3O_4@PDA@BSA-DOX Nanosystem for Enhanced Blood-Brain Barrier Penetration and Synergistic Glioblastoma Theranostic

Pejman Shahrokhi
Hormozgan University of Medical Sciences
Hamid Amiri Heydari
Hormozgan University of Medical Sciences
Mehdi Abedi
Shiraz University of Medical Sciences
Zahra Sobhani
Shiraz University of Medical Sciences, Shiraz, Iran
Mahvash Dehghankhold
Mahvash.dehghankhold@hums.ac.ir

Hormozgan University of Medical Sciences

Article

Keywords:

Posted Date: July 23rd, 2026

DOI: https://doi.org/10.21203/rs.3.rs-10204210/v1

License: This work is licensed under a Creative Commons Attribution 4.0 International License.
Read Full License

Additional Declarations: No competing interests reported.

Abstract

The treatment of glioblastoma multiforme (GBM) is severely hindered by the blood-brain barrier (BBB), which excludes approximately 98% of small-molecule drugs from the central nervous system. This study describes the design of an intelligent, albumin-coated magnetic nanosystem (Fe_3O_4@PDA@BSA-DOX) capable of crossing the BBB for integrated T2-weighted magnetic resonance imaging (MRI) and synergistic chemo-photothermal therapy. By leveraging endogenous albumin transport pathways and near-infrared (NIR) responsiveness, the system offers a high-precision approach to treating brain tumors.

Hemocompatibility assays showed that while Fe_3O_4@PDA extended activated partial thromboplastin time (aPTT), the BSA coating successfully restored coagulation times to normal ranges, ensuring safety. 3-(4,5-dimethylthiazol-2-yl)-2,5-diphenyltetrazolium bromide (MTT) assays demonstrated that the synergistic effect of the DOX-loaded nanocarrier combined with NIR irradiation reduced U87 cell viability to below 30%, significantly outperforming monotherapies. Furthermore, in vivo MRI confirmed successful BBB penetration of the nanosystem in the treated group with Fe_3O_4@PDA@BSA compared to the Fe_3O_4@PDA group. These findings highlight the potential of Fe_3O_4@PDA@BSA-DOX as a multifunctional candidate for enhanced GBM theranostics.

1. Introduction

Treatment of central nervous system (CNS) disorders faces significant obstacles due to the blood-brain barrier (BBB), a specialized protective interface that rigorously governs molecular exchange between the circulatory system and brain tissue. The BBB restricts approximately 98% of small-molecule drugs and virtually all large therapeutic agents from penetrating the CNS, leading to suboptimal therapeutic outcomes and increased systemic toxicity.[1–3]

Malignant brain tumors, particularly glioblastoma multiforme (GBM), are characterized by aggressive growth, high invasiveness, and poor prognosis, with a median survival of only 12–15 months despite multimodal treatments.[4–6] Traditional chemotherapy requires high systemic doses to achieve therapeutic concentrations in the brain, often resulting in severe off-target toxicity and limited efficacy. Nanotechnology emerges as a promising strategy to address these limitations through targeted delivery, controlled release, and multifunctional theranostic.[7,8]

Albumin, the most abundant plasma protein in human circulation, offers an exceptional biomimetic pathway for CNS delivery. Its prolonged half-life is governed by FcRn-mediated recycling, while glycoprotein 60 (gp60)-mediated transcytosis actively facilitates endothelial transport into the brain parenchyma and tumor microenvironments.[9–11] These properties confer exceptional biocompatibility and make albumin an ideal "Trojan Horse" coating for nanocarriers aiming to bypass the BBB. To further ensure precise therapeutic delivery and minimize premature drug leakage during systemic circulation, the integration of stimuli-responsive linkers is highly advantageous. In this context, utilizing 4,4'-azobis (4-cyanovaleric acid) (AZO) linkers combined with the photothermal properties of polydopamine (PDA)

provides a reliable, dual-responsive mechanism for on-demand drug release.[12–14] This strategy ensures that the therapeutic payload remains securely attached during BBB transcytosis and is only triggered locally within the tumor microenvironment upon near-infrared (NIR) irradiation or acidic conditions. In this study, we designed a novel multifunctional albumin-coated magnetic nanosystem (Fe_3O_4@PDA@BSA-DOX) for integrated T_2-weighted magnetic resonance imaging (MRI) and synergistic chemo-photothermal therapy of GBM. By exploiting endogenous albumin transport pathways for BBB penetration and utilizing NIR-responsive linkers for spatiotemporal drug release, this platform provides a precise theranostic strategy. The BBB-penetration capability and biosafety of this system were successfully validated in vivo, laying a strong foundation for targeted glioblastoma interventions.

2. Results

2.1. Physicochemical Characterization

The FTIR analysis of the Fe_3O_4@PDA@BSA platform revealed specific absorption bands: PDA-related peaks at 1510 and 1333 cm^{-1}, and BSA-associated amide I and II bands at 1647 and 1550 cm^{-1}. Upon DOX conjugation, additional peaks appeared at 1735 cm^{-1} (ester C = O) and 2240 cm^{-1} (C ≡ N). XRD patterns displayed diffraction peaks at 2θ angles of 30.4°, 36.6°, 43.3°, 53.8°, 57.6°, and 63.1°, corresponding to the (220), (311), (400), (422), (511), and (440) planes of magnetite.[15,16]

Morphological observations via TEM and FESEM showed spherical nanoparticles with a mean diameter of 98 ± 7.1 nm (Fig. 2). The EDX spectra confirmed the presence of C, N, O, and Fe in Fe_3O_4@PDA, while the Fe_3O_4@PDA@BSA sample showed an additional Sulfur (S) content of 0.29%. Magnetization measurements (VSM) yielded saturation magnetization (Ms) values of 87.8, 66.9, and 55.2 emu/g for Fe_3O_4, Fe_3O_4@PDA, and Fe_3O_4@PDA@BSA, respectively.

2.2. Drug Loading, Stimuli-Responsive Release, and Release Kinetics

The conjugation yield of AZO-DOX was 98.3%, with a calculated drug loading efficiency of 91.87%. Conductometric titration determined the free carboxylic acid concentration to be 18.6 μmol/g.

Under NIR laser irradiation, the temperature of the nanoparticle dispersion (200 μg/mL) rose from 29°C to 47°C within 10 minutes. In vitro release studies at 24 h showed cumulative DOX release rates of 25.5% (pH 7.4), 35.6% (pH 6.4), and 41.3% (pH 5.7). Under combined pH 5.7 and NIR laser exposure, the release reached a maximum of 71.9%.

The DOX release profiles from the Fe_3O_4@PDA@BSA-DOX nanosystem in the absence and presence of NIR laser irradiation across various pH media (7.4, 6.4, and 5.7) were evaluated using mathematical kinetic models, including zero-order, first-order, Higuchi, and Korsmeyer–Peppas (Fig. 3 and Fig. 4).[17] All evaluated groups exhibited significantly enhanced drug release in acidic environments compared to

physiological pH (7.4). This pH-responsive behavior is likely attributable to the protonation of the physically adsorbed DOX and the dissociation of the coordinate/covalent bonds under acidic conditions, coupled with the intrinsically higher solubility of DOX in low-pH media.

Notably, the formulations demonstrated a sustained release pattern over 24 hours without any significant initial burst release. To elucidate the underlying release mechanisms, the experimental data were fitted to the aforementioned kinetic models. As summarized in Table 1, the release profiles best fitted the Higuchi equation, yielding the highest correlation coefficients (R^2) in both the presence and absence of laser irradiation. The strong fit to the Higuchi model suggests that DOX release is primarily governed by diffusion through the nanocarrier matrix.

Furthermore, the Korsmeyer–Peppas model was applied to further delineate the diffusion mechanism. According to this model, the release exponent (n) at pH 5.7 and 6.4 (both with and without laser exposure) ranged between 0.45 and 0.89 ($0.45 < n < 0.89$), indicative of anomalous (non-Fickian) diffusion. Conversely, at pH 7.4, the n values fell between 0.89 and 1.0 ($0.89 < n < 1$), suggesting that the drug release follows a zero-order, non-Fickian Case II transport.[18–20] Case II transport typically occurs when the rate of solvent diffusion significantly exceeds the polymer chain relaxation rate.[21]

Table 1
Release-kinetic parameters and correlation coefficients (R2) of Fe_3O_4@PDA@BSA-DOX Nanosystem in the absent and present of laser beam for various mathematical models in different release medium pH

Release medium pH		Zero-order		First-order		Higuchi		Korsmeyer–Peppas	
		K_0	R^2	Q_{inf}	R^2	K_h	R^2	n	R^2
In the absence of laser beam	7.4	2.77	0.903	0.228	0.713	11.169	0.970	0.897	0.932
	6.4	3.69	0.901	0.205	0.741	14.891	0.967	0.801	0.946
	5.7	4.02	0.902	0.188	0.743	16.225	0.970	0.730	0.951
In the presence of laser beam	7.4	6.625	0.891	0.304	0.674	23.85	0.940	0.965	0.833
	6.4	7.430	0.844	0.227	0.642	27.05	0.908	0.887	0.811
	5.7	8.560	0.823	0.256	0.621	31.29	0.893	0.827	0.793

2.3. In Vitro and In Vivo Biological Performance

2.3.1. Evaluation of Blood Coagulation (PT and aPTT)

The results of the coagulation assays indicated that the nanoparticles interacted differently with the extrinsic and intrinsic pathways. PT: No significant differences were observed in the PT values for any of the nanoparticle formulations compared to the control group. This suggests that the Fe_3O_4@PDA@BSA system does not interfere with the extrinsic coagulation pathway.

aPTT: For Fe_3O_4@PDA nanoparticles, a concentration-dependent increase in aPTT was observed, with a significant delay in clotting time at 100 ~ μg/mL. However, the application of the BSA coating in the Fe_3O_4@PDA@BSA group effectively mitigated this effect, bringing the aPTT values back to the normal range (~ 15.5 ~ s) (Fig. 5).[22,23]

2.3.2. In Vitro Cytotoxicity Evaluation by MTT Assay

Figure 6 illustrates the cytotoxicity profiles of various nanoparticle (NP) formulations on U87 cell lines evaluated via an MTT assay after a 24-hour incubation period. The experimental groups comprised Fe_3O_4@PDA@BSA, Fe_3O_4@PDA@BSA-DOX, and free DOX, evaluated both in the presence and absence of laser irradiation. The vehicle control Fe_3O_4@PDA@BSA exhibited negligible toxicity across the tested concentration range, confirming its biocompatibility. At lower concentrations, no significant difference in cell viability was observed for Fe_3O_4@PDA@BSA regardless of laser exposure. However, at concentrations exceeding 5 μg/mL, laser irradiation significantly potentiated the cytotoxicity of these blank NPs compared to their non-irradiated counterparts, which is attributable to the robust photothermal conversion capability of the PDA shell .[24–26] Furthermore, the therapeutic efficacy was markedly enhanced with the drug-loaded system (Fe_3O_4@PDA@BSA-DOX) under laser irradiation, demonstrating substantial cytotoxicity even at minimal doses. Notably, within the U87 cell line, the combination of Fe_3O_4@PDA@BSA-DOX and laser irradiation surpassed the efficacy of free DOX.[27] Overall, the statistical variance in cytotoxicity between free DOX and the irradiated, DOX-loaded nanocarriers did not reach statistical significance in U87 cells.

2.3.3. In Vivo MRI

Given the high r_2 relaxivity typically associated with superparamagnetic iron oxide nanoparticles, we conducted T_2-weighted MRI in healthy mice.[28–30] Following intravenous administration of Fe_3O_4@PDA and Fe_3O_4@PDA@BSA nanoparticles, the animals underwent MRI scanning 24 hours after injection. MRI scans revealed clear signal enhancement in the brain of the Fe_3O_4@PDA@BSA-treated group, confirming successful BBB penetration (Fig. 7).

3. Discussion

In our previous research, the Fe_3O_4@PDA@BSA-DOX nanosystem demonstrated exceptional efficacy in treating melanoma. However, translating this success to primary brain malignancies like GBM requires overcoming the BBB—a formidable physiological barrier that restricts the vast majority of therapeutic agents. Therefore, a "smart" carrier is required that transcends simple physical localization.

The Fe_3O_4@PDA@BSA nanosystem functions as a biomimetic gateway. The nanosystem's albumin corona actively engages gp60 (albondin) and neonatal Fc receptors (FcRn) expressed on brain endothelial cells. This interaction actively facilitates transcytosis into the brain parenchyma. MRI scans confirmed this mechanism, revealing clear signal enhancement in the brains of the Fe_3O_4@PDA@BSA-

treated group. In contrast, the intermediate Fe_3O_4@PDA nanoparticles lacked any detectable signal attenuation. This binary distinction establishes a strong correlation between the BSA outer layer and successful in vivo cerebral localization.

Compared to other conventional BBB-crossing strategies, such as standard PEGylation or transferrin-conjugated liposomes, our albumin-based platform offers distinct advantages. While PEGylation improves circulation time, it often hinders cellular uptake (the "PEG dilemma").[31–33] Conversely, the BSA corona not only provides stealth properties and mitigates coagulation interference (as evidenced by our normalized aPTT results), but it also actively drives receptor-mediated cellular internalization without the need for complex synthetic ligands.

It is noteworthy that while the in vitro cytotoxicity of the irradiated Fe_3O_4@PDA@BSA-DOX did not statistically surpass that of free DOX in U87 cells, the true clinical value of this nanoplatform lies in its systemic profile. Free DOX exhibits severe dose-limiting cardiotoxicity and completely fails to cross the BBB in vivo.[34–37] Our targeted system safely sequesters the drug during circulation, crosses the BBB efficiently, and restricts payload release to the tumor site via NIR and pH triggers, thereby maximizing safety and localized efficacy.

4. Conclusion and Future Perspectives

Surface functionalization with BSA primes the nanoplatform for receptor-mediated transcytosis. This mechanism is expected to drive selective accumulation within the tumor microenvironment, sparing healthy brain tissue. Consequently, we propose that this albumin-based nanocarrier not only facilitates targeted delivery to the intracranial tumor site but also synergizes with photothermal therapy to overcome the physiological barriers inherent in glioma, warranting further investigation in orthotopic glioblastoma models.

5. Materials and Methods

5.1. Reagents and Materials

High-purity reagents including iron salts (FeCl3·6H2O, FeCl2·4H2O), dopamine, Bovine Serum Albumin (BSA), Doxorubicin HCl (DOX), and coupling agents (NHS, EDAC HCl, AZO) were procured from Sigma-Aldrich (USA). Standard solvents and buffer components such as DMF, CH_2Cl_2, and various phosphates were obtained from Merck (Germany).

5.2. Instrumentation

The structural and morphological properties of the synthesized nanoparticles (NPs) were characterized using X-ray diffraction (XRD, Bruker D8 Advanced), transmission electron microscopy (TEM, LEO-906E), and field emission scanning electron microscopy (FESEM, TESCAN MIRA). Elemental composition was verified via energy-dispersive X-ray spectroscopy (EDX), while magnetic properties were assessed using

a vibrating sample magnetometer (VSM, Kavier Kashan). Thermal stability was analyzed through thermogravimetric analysis (TGA, Perkin Elmer). Surface functional groups and iron content were determined by Fourier transform infrared spectroscopy (FTIR, Bruker Vertex 70) and inductively coupled plasma optical emission spectroscopy (ICP-OES, Optima 7300), respectively. Hydrodynamic size and Zeta potential were measured using dynamic light scattering (DLS) and ZETA-check (Colloid Metrics). Drug conjugation and MRI performance were evaluated using high-performance liquid chromatography (HPLC, Cecil Adept), ultraviolet-visible (UV-Vis) spectrophotometry (PG Instruments), and a Siemens MAGNETOM Avanto MRI system.

5.3. Preparation of Fe_3O_4@PDA@BSA Nanocomposite

Magnetic Fe_3O_4 cores were synthesized according to the method reported by Dehghankhold et al.[38] using a modified co-precipitation approach, followed by polydopamine coating and subsequent BSA surface functionalization. Briefly, $FeCl_2$ and $FeCl_3$ were reacted at 80°C under a nitrogen atmosphere with the pH adjusted to 10–11 using NH_4OH. The obtained Fe_3O_4 nanoparticles were coated with PDA in Tris buffer (pH 8.5) containing dopamine hydrochloride for 12 h, and then incubated in BSA/PBS solution (pH 7.4) at 30°C for 24 h to obtain Fe_3O_4@PDA@BSA NPs. The final nanoparticles were magnetically separated and quantified using the Bradford assay.

5.4. AZO-DOX Coupling and Loading

All the steps for conjugating DOX to AZO and subsequently loading AZO-DOX onto the nanocarrier have been reported in the previous work Briefly, the AZO-DOX linker was synthesized by activating the carboxylic groups of AZO with NHS/EDAC in acetone, followed by conjugation with DOX in DMF.[38] The degree of free carboxyl groups was determined via conductometric titration. For loading, the activated NHS-AZO-DOX complex was reacted with Fe_3O_4@PDA@BSA in phosphate buffer (pH 8.0) for 24 h.

The drug conjugation (AZO-DOX) and loading efficiencies (Fe_3O_4@PDA@BSA NPs) were determined indirectly via calibration curves by monitoring the supernatant; HPLC was utilized to quantify unreacted DOX, whereas UV-Vis spectroscopy (499 nm) was employed to measure unbound AZO-DOX.

5.5. Photothermal and Drug Release Studies

The photothermal response of the NPs was evaluated by exposing aqueous dispersions to NIR laser (2 W) for 10 min, recording temperature changes every 60 s. To assess drug release, the Fe_3O_4@PDA@BSA-DOX nanocomposite was incubated in PBS at varying pH levels (5.7, 6.4, and 7.4). The impact of NIR-triggered release was studied by periodically irradiating the samples (2.0 W/cm² for 5 min) and measuring the released DOX concentration with a UV spectrophotometer at 480 nm .

5.6 Hemocompatibility Assays: PT and aPTT

The impact of the synthesized nanoparticles (Fe_3O_4@PDA, and Fe_3O_4@PDA@BSA) on the blood coagulation cascade was evaluated using Prothrombin Time (PT) and activated Partial Thromboplastin Time (aPTT) assays. Briefly, fresh whole blood from healthy volunteers was collected in tubes containing

3.2% sodium citrate as an anticoagulant. Platelet-poor plasma (PPP) was obtained by centrifugation at 3000 ~ g for 10 min.

All blood sampling protocols were performed in accordance with the Declaration of Helsinki guidelines and regulations, and were officially approved by the Ethics Committee of Shiraz University of Medical Sciences, Iran (Approval Number: IR.SUMS.AEC.1401.052). Written informed consent was obtained from all healthy volunteers prior to their participation in the study.

Various concentrations of the nanoparticles (ranging from 0.25 to 100 ~ μg/mL) were incubated with the PPP at 37°C for 30 min to allow for potential interactions with coagulation factors. Following incubation, the PT and aPTT were measured using an automated coagulation analyzer with the corresponding commercial reagents. Plasma treated with phosphate-buffered saline (PBS) served as the negative control.

5.7 In Vitro Cytotoxicity Evaluation by MTT Assay

To assess the cytotoxic effects of the prepared nanocarrier systems, a colorimetric MTT (3 − 2,5-diphenyltetrazolium bromide) assay was performed according to established protocols.[39] The MTT assay relies on mitochondrial dehydrogenase activity that reduces the yellow tetrazolium salt to purple formazan crystals in metabolically active cells, which can be quantified spectrophotometrically.

Human glioblastoma U87 cells were cultured in Dulbecco's Modified Eagle Medium (DMEM) supplemented with 10% fetal bovine serum and 1% penicillin/streptomycin at 37°C in a humidified atmosphere containing 5% CO_2. Cells were seeded at a density of 1×10^4 cells per well in 96-well plates and allowed to adhere for 24 h.

After attachment, cells were treated with various formulations (Fe_3O_4@PDA@BSA, Fe_3O_4@PDA@BSA-DOX, free DOX, with/without NIR laser) at predetermined concentrations: 1, 2, 5, 10, and 20 μg/mL (on a DOX basis). Following a 24-h incubation, 100 μL of MTT solution (0.5 mg/mL in PBS) was added to each well and incubated for 4 h to allow formazan formation.

After incubation, the media was carefully removed, and 100 μL dimethyl sulfoxide (DMSO) was added to each well to dissolve the formazan crystals. Optical density was measured at 570 nm using a microplate reader. Cell viability was calculated relative to untreated control cells using the formula:

Cell viability (%) = (OD treatment / OD control) × 100.

5.8. In Vivo MRI

All biological procedures and animal handling were performed in accordance with the protocols approved by the Animal Center of Shiraz University of Medical Sciences, Iran (IR.SUMS. AEC.1401.052). To evaluate the ability of the nanoparticles to cross the BBB, healthy female C57BL/6 mice (6–8 weeks old) were obtained from the Animal Center of Shiraz University of Medical Sciences.[40,41] The mice were

randomly divided into two experimental groups (n = 4 per group): (1) mice receiving Fe_3O_4@PDA, and (2) mice receiving Fe_3O_4@PDA@BSA nanoparticles.

Each animal was injected intravenously with 200 µL of either nanoparticle suspension (2 mg/mL). Twenty-four hours post-injection, the mice were anesthetized and subjected to in vivo MRI using a 1.5 T clinical MRI scanner (Siemens MAGNETOM Avanto, Germany) equipped with a dedicated small animal radiofrequency (RF) coil. T2-weighted (T2w) turbo spin-echo (TSE) coronal images were acquired to assess cerebral accumulation. The primary imaging parameters were set as follows: repetition time (TR) = [3500] ms, echo time (TE) = [89] ms, slice thickness = [1.5] mm, field of view (FOV) = [80 × 80] mm, and matrix size = [256 × 256]. Additionally, corresponding gradient echo images were obtained in the same plane to further emphasize the signal attenuation (negative contrast) induced by the superparamagnetic iron oxide cores in the brain parenchyma.

Following the completion of the imaging protocols, all animals were humanely sacrificed. Euthanasia was performed via an intraperitoneal overdose injection of Ketamine (150 mg/kg) and Xylazine (15 mg/kg). Successful euthanasia was verified by confirming the complete loss of respiratory activity, cardiac arrest, and the absence of hind-paw and corneal reflexes.

5.9. Statistical Analysis

All quantitative data were expressed as the mean ± standard deviation (SD) or standard error (SE), as appropriate. Statistical analyses were performed using GraphPad Prism software (version [8.0], GraphPad Software, San Diego, CA, USA). Comparisons between two independent groups were evaluated using an unpaired Student's t-test. For comparisons involving three or more groups, a one-way or two-way analysis of variance (ANOVA) was applied, followed by Tukey's post-hoc test for multiple comparisons. A p-value of less than 0.05 was considered statistically significant. In all figures, statistical significance is denoted as *$p < 0.05$, **$p < 0.01$, ***$p < 0.001$, and ****$p < 0.0001$, while "NS" indicates non-significant differences.

Declarations

Data availability

The datasets generated and/or analysed during the current study are available from the corresponding author on reasonable request.

Acknowledgements

This research was supported by Shiraz University of Medical Sciences (grant No. 25131). The authors would also like to thank the Animal Center of Shiraz University of Medical Sciences for their assistance with the in vivo imaging facilities.

Funding Declaration

This study was supported by Shiraz University of Medical Sciences (grant number 25131). The authors declare that no additional funds, grants, or other support were received during the preparation of this manuscript.

CRediT authorship contribution statement

Mahvash Dehghankhold: Supervision, Conceptualization, Methodology, Investigation, Formal analysis, Data curation, Writing – original draft, Writing – review & editing. **Hamid Amiri Hidari:** Methodology, Investigation, Formal analysis, Data curation, Writing – original draft, Writing – review & editing. **Mehdi Abedi:** Methodology, Formal analysis. **Pegman Shahrokhi:** Methodology, Formal analysis. **Zahra Sobhan:** Investigation, Formal analysis, Data curation, Writing – original draft, Writing – review & editing.

Declaration of competing interest

The authors declare that they have no known competing financial interests or personal relationships that could have appeared to influence the work reported in this paper.

Ethical approval

All biological procedures and animal handling were performed in accordance with the ethical guidelines and protocols approved by the Animal Center of Shiraz University of Medical Sciences, Iran (Approval Number: IR.SUMS.AEC.1401.052). All experiments were conducted in compliance with the ARRIVE guidelines for the reporting of in vivo experiments.

References

1. Wu, D. *et al.* The blood-brain barrier: Structure, regulation, and drug delivery. *Signal Transduct Target Ther* **8**, 217 (2023). https://doi.org/10.1038/s41392-023-01481-w
2. Cornelissen, F. M. G. *et al.* Explaining blood-brain barrier permeability of small molecules by integrated analysis of different transport mechanisms. *J Med Chem* **66**, 7253–7267 (2023). https://doi.org/10.1021/acs.jmedchem.2c01824
3. Zheng, X. *et al.* Current non-invasive strategies for brain drug delivery: Overcoming blood-brain barrier transport. *Mol Biol Rep* **51**, 25 (2023). https://doi.org/10.1007/s11033-023-08968-3
4. Dhingra, S., Koshy, M. & Korpics, M. Limited survival benefit in patients diagnosed with glioblastoma post-2016: A seer population based registry analysis. *J Cancer Res Clin Oncol* **151**, 179 (2025). https://doi.org/10.1007/s00432-025-06171-4
5. Tini, P. *et al.* Timing matters: Overall treatment time, radiotherapy interruptions, and outcomes in glioblastomas-prognostic significance in different biological sub-groups. *J Neurooncol* **175**, 1261–1269 (2025). https://doi.org/10.1007/s11060-025-05215-6
6. Stupp, R. *et al.* Radiotherapy plus concomitant and adjuvant temozolomide for glioblastoma. *N Engl J Med* **352**, 987–996 (2005). https://doi.org/10.1056/NEJMoa043330

7. Saxena, S., Kaur, J., Singh, T. G., Kumar, M. & Awasthi, A. Beyond the brain barrier: Hybrid nanoparticles orchestrating intelligent neuro-theranostics. *Adv Colloid Interface Sci* **356**, 103954 (2026). https://doi.org/10.1016/j.cis.2026.103954
8. Shi, Y. *et al.* Magnetic resonance imaging-guided thermoradiotherapy for glioblastoma using GD(3+)-loaded melanin nanoparticles reverses anoikis resistance through the ITGA5-PI3K/AKT axis. *Colloids Surf B Biointerfaces* **266**, 115874 (2026). https://doi.org/10.1016/j.colsurfb.2026.115874
9. Sorets, A. G., Rosch, J. C., Duvall, C. L. & Lippmann, E. S. Caveolae-mediated transport at the injured blood-brain barrier as an underexplored pathway for central nervous system drug delivery. *Curr Opin Chem Eng* **30**, 86–95 (2020). https://doi.org/10.1016/j.coche.2020.08.009
10. Ding, L., Kshirsagar, P., Agrawal, P. & Murry, D. J. Crossing the blood-brain barrier: Innovations in receptor- and transporter-mediated transcytosis strategies. *Pharmaceutics* **17** (2025). https://doi.org/10.3390/pharmaceutics17060706
11. Haqqani, A. S., Belanger, K. & Stanimirovic, D. B. Receptor-mediated transcytosis for brain delivery of therapeutics: Receptor classes and criteria. *Front Drug Deliv* **4**, 1360302 (2024). https://doi.org/10.3389/fddev.2024.1360302
12. Wu, J. *et al.* Light-responsive smart nanoliposomes: Harnessing the azobenzene moiety for controlled drug release under near-infrared irradiation. *ACS Appl Mater Interfaces* **16**, 56850–56861 (2024). https://doi.org/10.1021/acsami.4c13549
13. Wang, M., Wang, T., Wang, D., Jiang, W. & Fu, J. Acid and light stimuli-responsive mesoporous silica nanoparticles for controlled release. *Journal of Materials Science* **54**, 6199–6211 (2019). https://doi.org/10.1007/s10853-019-03325-x
14. Yao, C. *et al.* Near-infrared-triggered azobenzene-liposome/upconversion nanoparticle hybrid vesicles for remotely controlled drug delivery to overcome cancer multidrug resistance. *Adv Mater* **28**, 9341–9348 (2016). https://doi.org/10.1002/adma.201503799
15. Asab, G., Zereffa, E. A. & Abdo Seghne, T. Synthesis of silica-coated Fe_3O_4 nanoparticles by microemulsion method: Characterization and evaluation of antimicrobial activity. *Int J Biomater* **2020**, 4783612 (2020). https://doi.org/10.1155/2020/4783612
16. Winsett, J. *et al.* Quantitative determination of magnetite and maghemite in iron oxide nanoparticles using mössbauer spectroscopy. *SN Applied Sciences* **1** (2019). https://doi.org/10.1007/s42452-019-1699-2
17. Bediako, E. G. *et al.* Modified halloysite nanoclay as a vehicle for sustained drug delivery. *Heliyon* **4**, e00689 (2018). https://doi.org/10.1016/j.heliyon.2018.e00689
18. Uskokovic, V. Mechanism of formation governs the mechanism of release of antibiotics from calcium phosphate nanopowders and cements in a drug-dependent manner. *J Mater Chem B* **7**, 3982–3992 (2019). https://doi.org/10.1039/c9tb00444k
19. Zhu, C. *et al.* A ph-responsive composite hydrogel based on konjac glucomannan and its oxidized derivatives: Synthesis, characterization and swelling behavior. *Curr Res Food Sci* **12**, 101452 (2026). https://doi.org/10.1016/j.crfs.2026.101452

20. Sobitharani, P., Anandam, S., Mohan Varma, M., Vijaya Ratna, J. & Shailaja, P. Investigation on dissolution pattern and mathematical modeling of drug release of quercetin by complexation with cyclodextrin nanosponges. *Asian Journal of Pharmaceutical and Clinical Research*, 260–264 (2019). https://doi.org/10.22159/ajpcr.2019.v12i5.32864
21. Ganji, F., Vasheghani, F. S. & Vasheghani, F. E. Theoretical description of hydrogel swelling: A review. *Iranian Polymer Journal* **19**, 375–398 (2010).
22. Milic, M. *et al.* Response of platelets to silver nanoparticles designed with different surface functionalization. *J Inorg Biochem* **224**, 111565 (2021). https://doi.org/10.1016/j.jinorgbio.2021.111565
23. Sharma, I., Sharaf, M. G., Pawar, A., Lockwood, E. & Unsworth, L. D. Albumin coatings for counteracting uremic metabolites effects on host responses to biomaterials. *Front Bioeng Biotechnol* **13**, 1704352 (2025). https://doi.org/10.3389/fbioe.2025.1704352
24. Acter, S., Moreau, M., Ivkov, R., Viswanathan, A. & Ngwa, W. Polydopamine nanomaterials for overcoming current challenges in cancer treatment. *Nanomaterials (Basel)* **13** (2023). https://doi.org/10.3390/nano13101656
25. Xu, N. *et al.* Fe(iii)-chelated polydopamine nanoparticles for synergistic tumor therapies of enhanced photothermal ablation and antitumor immune activation. *ACS Appl Mater Interfaces* **14**, 15894–15910 (2022). https://doi.org/10.1021/acsami.1c24066
26. Zhu, Z. & Su, M. Polydopamine nanoparticles for combined chemo- and photothermal cancer therapy. *Nanomaterials (Basel)* **7** (2017). https://doi.org/10.3390/nano7070160
27. Lu, L. *et al.* Constructing nanocomplexes by multicomponent self-assembly for curing orthotopic glioblastoma with synergistic chemo-photothermal therapy. *Biomaterials* **279**, 121193 (2021). https://doi.org/10.1016/j.biomaterials.2021.121193
28. Zhao, Z. *et al.* Octapod iron oxide nanoparticles as high-performance t(2) contrast agents for magnetic resonance imaging. *Nat Commun* **4**, 2266 (2013). https://doi.org/10.1038/ncomms3266
29. Laissy, J. P. Editorial for "comparison of three ultrasmall, superparamagnetic iron oxide nanoparticles for MRI at 3.0 t". *J Magn Reson Imaging* **57**, 1830–1831 (2023). https://doi.org/10.1002/jmri.28452
30. Cho, M. *et al.* Sensitive t2 mri contrast agents from the rational design of iron oxide nanoparticle surface coatings. *The Journal of Physical Chemistry C* **127**, 1057–1070 (2023). https://doi.org/10.1021/acs.jpcc.2c05390
31. Zalba, S., Ten Hagen, T. L. M., Burgui, C. & Garrido, M. J. Stealth nanoparticles in oncology: Facing the PEG dilemma. *J Control Release* **351**, 22–36 (2022). https://doi.org/10.1016/j.jconrel.2022.09.002
32. Pelaz, B. *et al.* Surface functionalization of nanoparticles with polyethylene glycol: Effects on protein adsorption and cellular uptake. *ACS Nano* **9**, 6996–7008 (2015). https://doi.org/10.1021/acsnano.5b01326

33. Tian, Y. *et al.* Engineering poly(ethylene glycol) nanoparticles for accelerated blood clearance inhibition and targeted drug delivery. *J Am Chem Soc* **144**, 18419–18428 (2022). https://doi.org/10.1021/jacs.2c06877
34. McGovern, K. *et al.* Abstract lb132: Doxorubicin impairs the blood-brain barrier in a microfluidic model of the human neurovascular unit. *Cancer Research* **86**, LB132–LB132 (2026). https://doi.org/10.1158/1538-7445.Am2026-lb132
35. Bhutani, V. *et al.* Doxorubicin-induced cardiotoxicity: A comprehensive update. *J Cardiovasc Dev Dis* **12** (2025). https://doi.org/10.3390/jcdd12060207
36. Dorostkar, H. *et al.* Reduction of doxorubicin-induced cardiotoxicity by co-administration of smart liposomal doxorubicin and free quercetin: In vitro and in vivo studies. *Pharmaceutics* **15** (2023). https://doi.org/10.3390/pharmaceutics15071920
37. Kostka, K. *et al.* The application of ultrasmall gold nanoparticles (2 nm) functionalized with doxorubicin in three-dimensional normal and glioblastoma organoid models of the blood-brain barrier. *Molecules* **29** (2024). https://doi.org/10.3390/molecules29112469
38. Dehghankhold, M. *et al.* A versatile theranostic magnetic polydopamine iron oxide nir laser-responsive nanosystem containing doxorubicin for chemo-photothermal therapy of melanoma. *Biomater Adv* **159**, 213797 (2024). https://doi.org/10.1016/j.bioadv.2024.213797
39. van Meerloo, J., Kaspers, G. J. & Cloos, J. Cell sensitivity assays: The MTT assay. *Methods Mol Biol* **731**, 237–245 (2011). https://doi.org/10.1007/978-1-61779-080-5_20
40. Wei, Z. *et al.* Non-contrast assessment of blood-brain barrier permeability to water in mice: An arterial spin labeling study at cerebral veins. *Neuroimage* **268**, 119870 (2023). https://doi.org/10.1016/j.neuroimage.2023.119870
41. Schaffenrath, J., Huang, S. F., Wyss, T., Delorenzi, M. & Keller, A. Characterization of the blood-brain barrier in genetically diverse laboratory mouse strains. *Fluids Barriers CNS* **18**, 34 (2021). https://doi.org/10.1186/s12987-021-00269-w

Figures

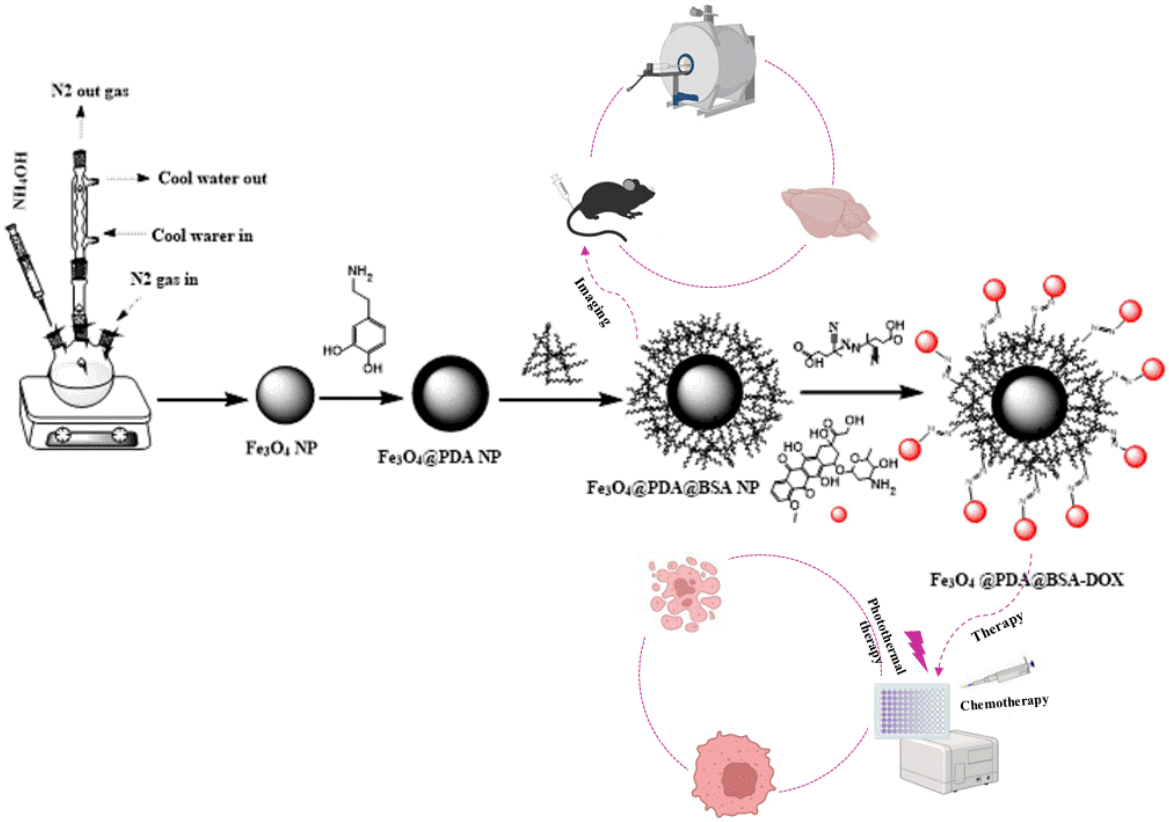


Figure 1

Illustration of the synthetic route for Fe3O4@PDA@BSA-DOX.

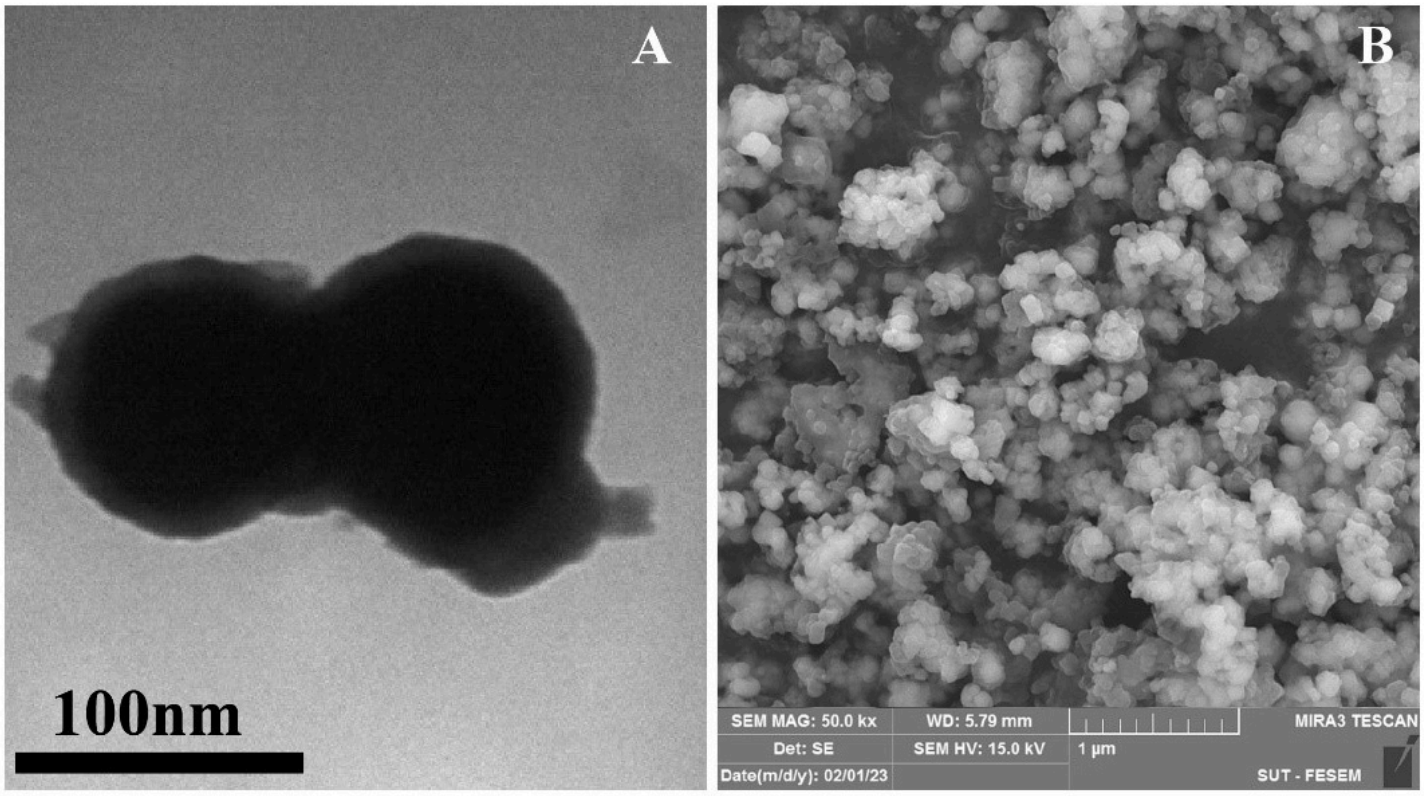


Figure 2

Morphology of Fe_3O_4@PDA@BSA nanoparticle. (A) TEM image of Fe_3O_4@PDA@BSA and (B) FESEM image of Fe_3O_4@PDA@BSA

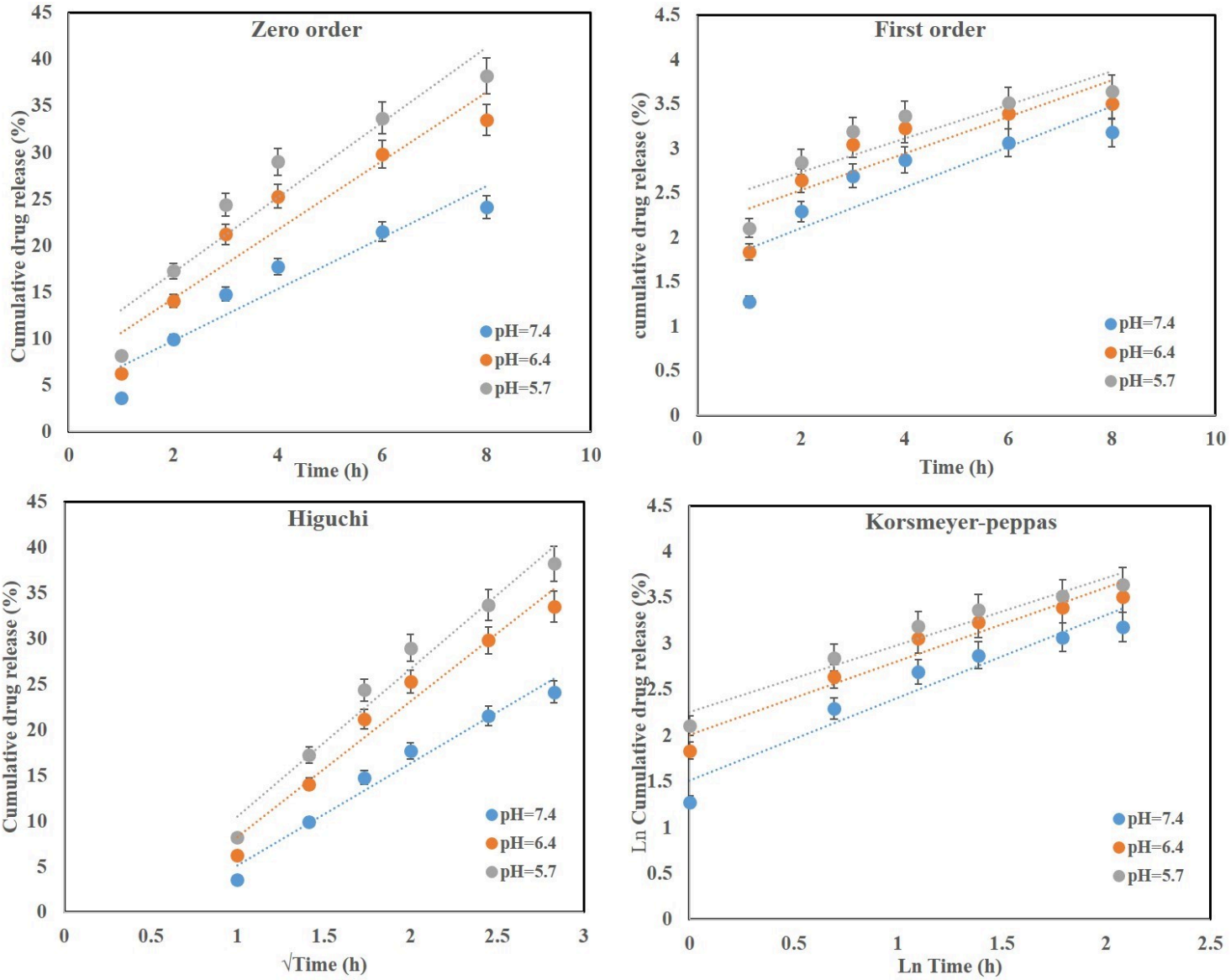


Figure 3

Drug-release profile from Fe_3O_4@PDA@BSA-DOX in the absence of laser in pH 7.4, pH 6.4 and pH 5.7 according to (A) zero-order, (B) first-order, (C) Higuchi, and (D) Korsmeyer–Peppas kinetic models.

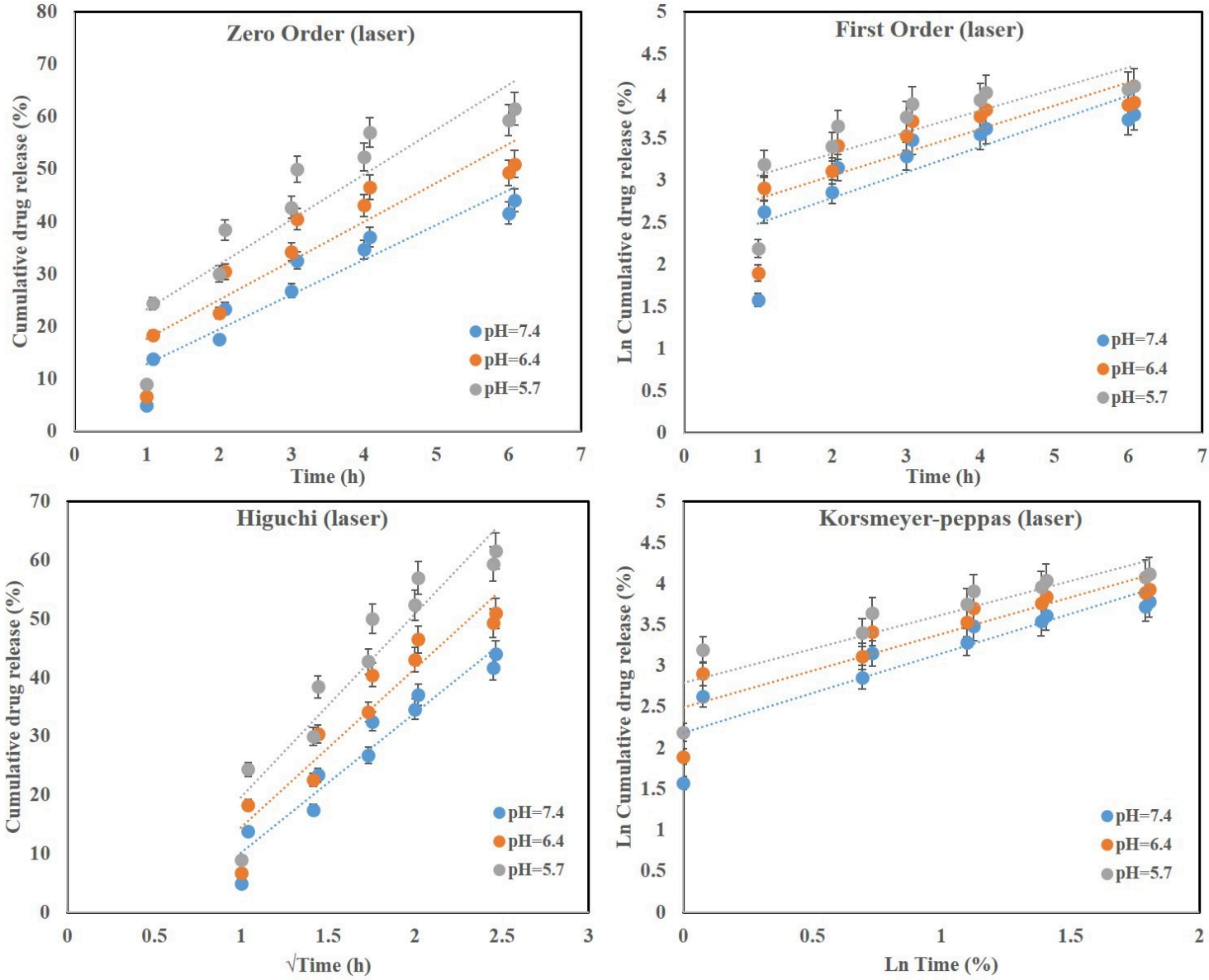


Figure 4

Drug-release profile from Fe_3O_4@PDA@BSA-DOX In the present of laser beam in pH 7.4, pH 6.4 and pH 5.7 according to (A) zero-order, (B) first-order, (C) Higuchi, and (D) Korsmeyer–Peppas kinetic models.

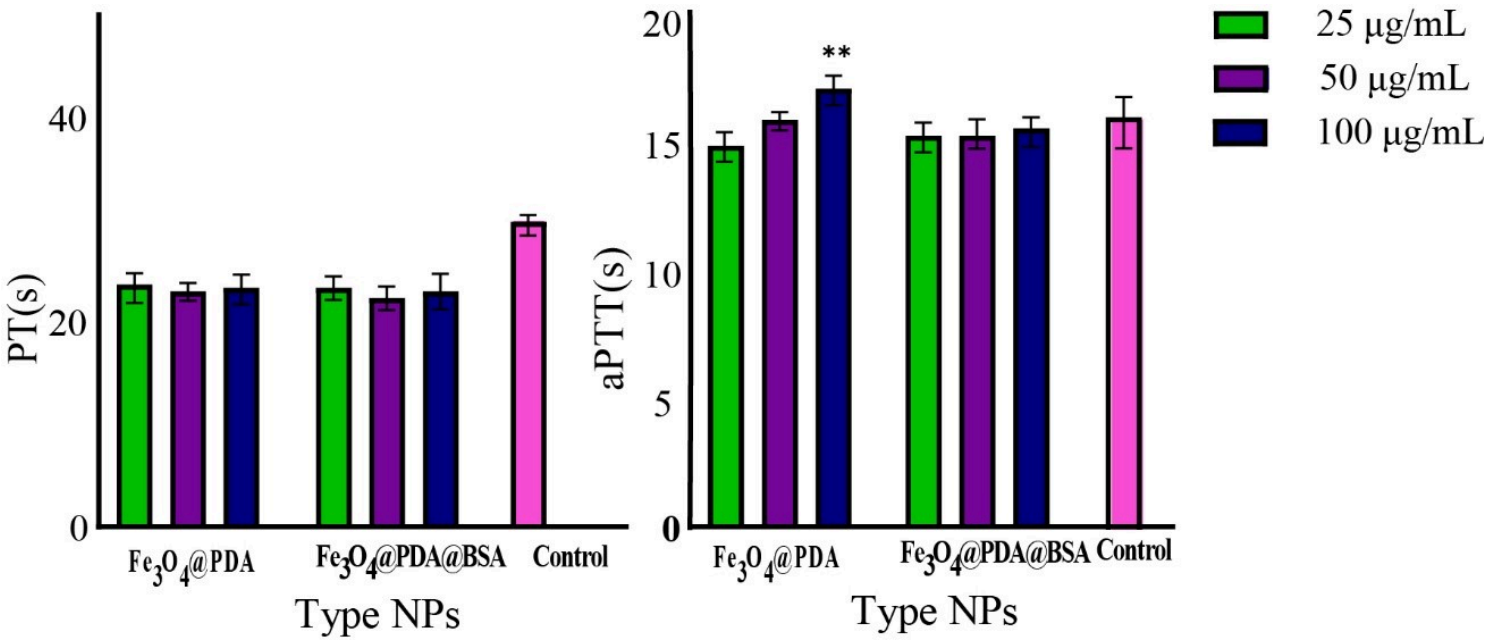


Figure 5

Prothrombin time (PT) and activated partial thromboplastin time (aPTT) were measured to evaluate the blood coagulation compatibility after incubating human plasma with Fe_3O_4@PDA and Fe_3O_4@PDA@BSA (at concentrations of 25, 50, and 100 μg/mL). PBS was employed as the negative control. Values represent the mean ± S.E. of at least 3 independent experiments; denotes statistical significance ($p < 0.01$) versus the control group.

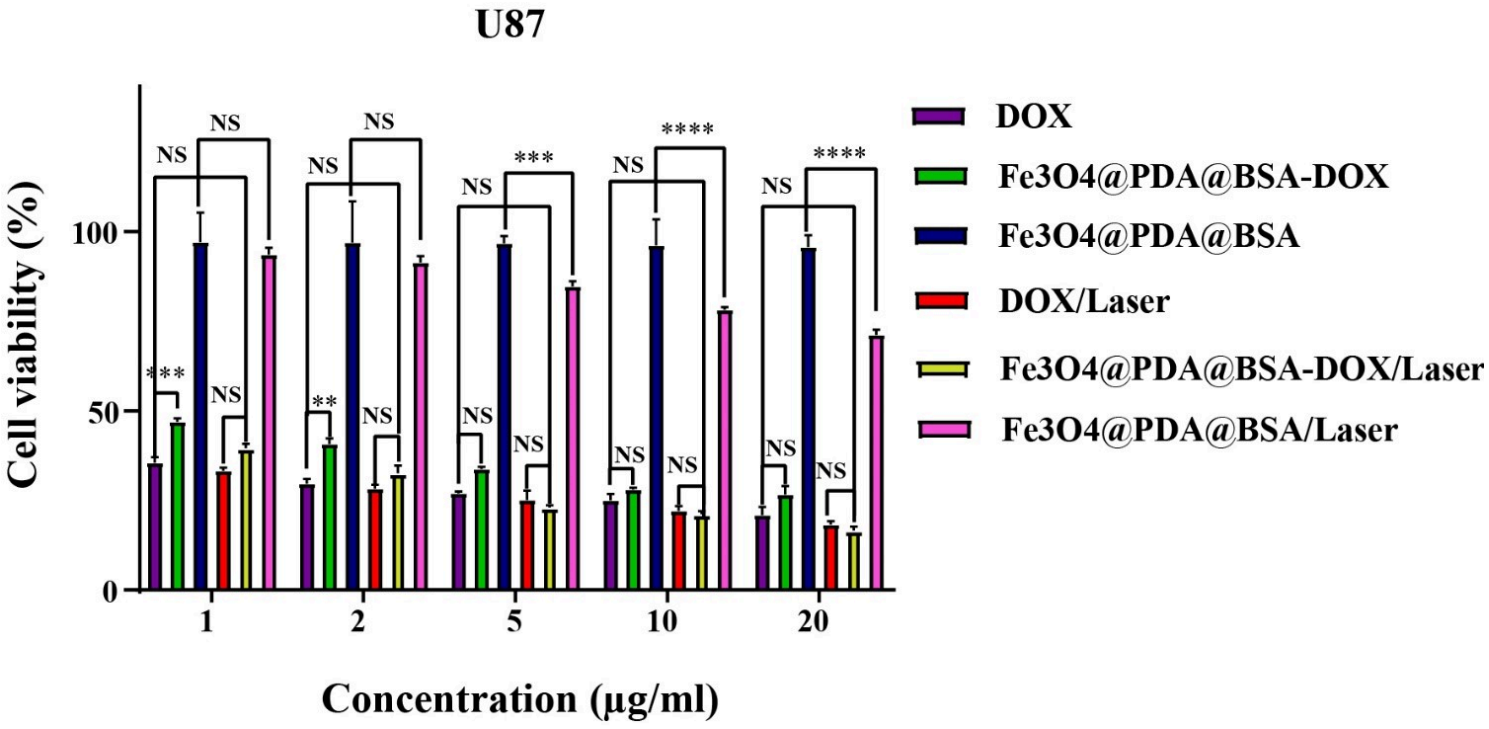


Figure 6

Cytotoxicity of various formulations in U87 cells. Cell viability was determined by MTT assay after 24 h of incubation with different concentrations of free DOX, Fe_3O_4@PDA@BSA–DOX, Fe_3O_4@PDA@BSA, DOX laser, Fe_3O_4@PDA@BSA–DOX-laser and PDA@BSA– laser nanoparticles, in the presence or absence of laser irradiation (808 nm). Data are presented as mean ± S.D. (n≥3). Statistical significance is indicated as follows: * p value ≤ 0.05, ** p value ≤ 0.01, *** p value ≤ 0.001 and **** p value ≤ 0.0001.

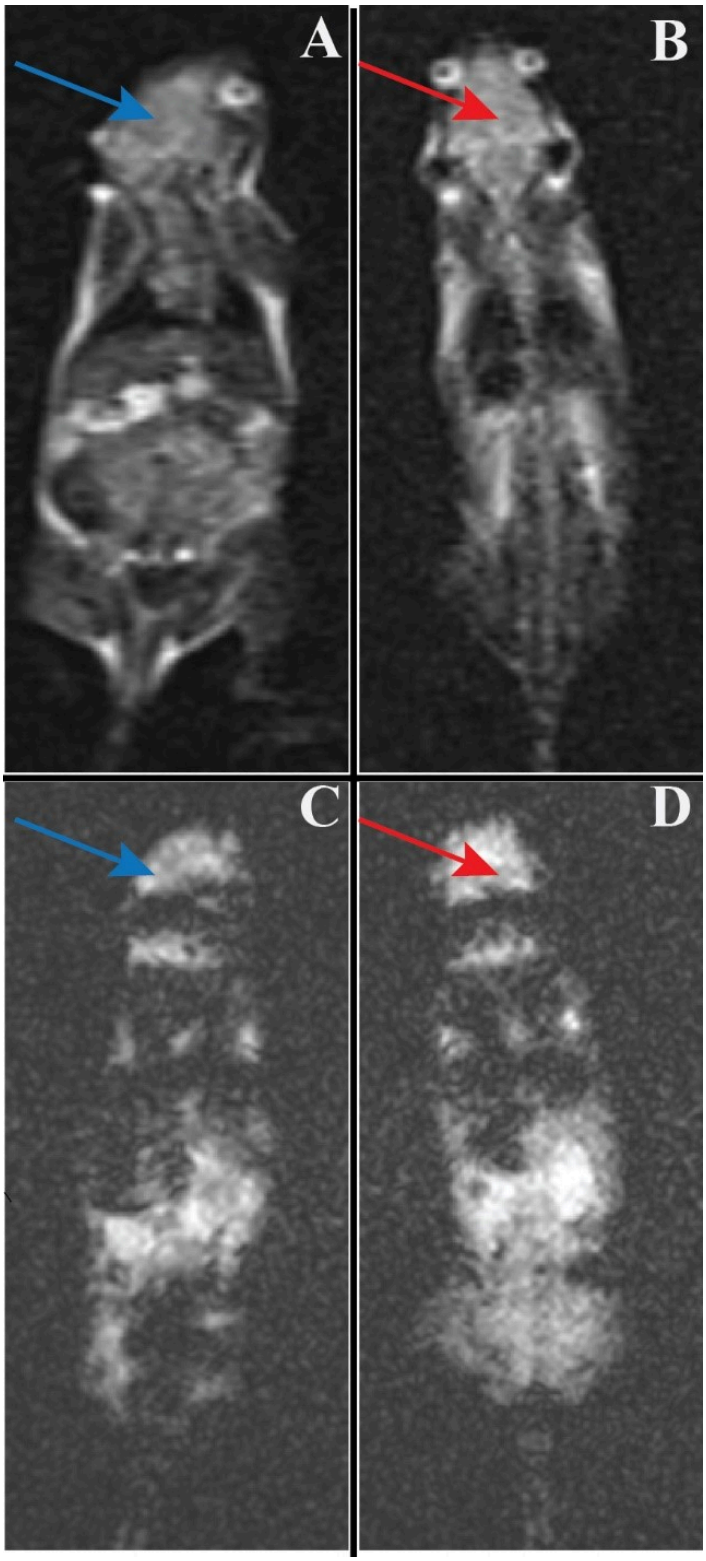


Figure 7

In Vivo Imaging of MNP Distribution in the Brain Using MRI. A,B) Coronal T2w images and corresponding gradient echo images (C, D) in the same plane, to enhance the visualization of contrast uptake in the brain. (A, C) Treated mice with Fe_3O_4@PDA@BSA, (B, D) Treated mice with Fe_3O_4@PDA